Drag Reduction Control for Flow over a Hump with Surface-Mounted Thermoacoustic Actuator

Chi-An Yeh[*], Phillip M. Munday[†], Kunihiko Taira[‡]

Florida State University, Tallahassee, FL

Matthew J. Munson[§]

U.S. Army Research Laboratory, Aberdeen Proving Ground, MD

Motivated by the recent development in fabricating graphene/carbon nanotube-based surface compliant loud speakers, the effectiveness of thermoacoustic actuators that locally introduce high-intensity acoustic waves for active flow control is examined by performing high-fidelity large eddy simulation for compressible flow over a wall-mounted hump at a Reynolds number of 0.5×10^6 and Mach number of 0.25. Based on performance characteristics of the grephene-based thermoacoustic actuators, high-frequency actuation around Helmholtz number of 3.0 is considered. We observe that the actuation is able to introduce small-scale perturbations to the shear layer in the separated flow and attenuate the formation of large scale spanwise vortices. This flow control technique elongates the recirculation zone and shifts the low-pressure region downstream of the hump. As a consequence, the drag on the hump is reduced by approximately 4.31% and 6.33% for two and three-dimensional simulation, respectively.

I.   Introduction

Drag reduction has long been a major motivation for application of active flow control,[1] which can be performed by injecting mass, momentum, or vorticity (or the combination thereof) in either a steady or unsteady fashion. Flow control actuation can be introduced by various types of devices,[2] such as the synthetic jets,[3] dielectric barrier discharge (DBD) plasma actuators,[4] or combustion powered actuators.[5] Among these applications, the bulkiness due to the weight and size of the actuator as well as the amount of power required to deliver the control perturbation into the flow field are two main issues that restrict the implementation of active flow control on full scale engineering systems.

To address the above two limitations, we consider the use of a novel speaker made of carbon nanotubes/graphene as a flow control actuator. A membrane of carbon nanotubes/graphene laid on a backing material such as paper under AC power has been shown to produce large-amplitude acoustic waves.[6] Rather than generating motion on the membrane itself to produce acoustic waves, the input AC current sinusoidally heats this membrane due to Joule heating and creates surface pressure disturbances within the surrounding fluid. This pressure disturbances are then propagated through the fluid field as high-intensity acoustic waves.[7,8] One of the attractive characteristics of this carbon-based sound-emitting device is its sheet-like arrangement that can be applied to essentially any surface, without occupying any internal space nor adding significant weight, which is similar to how DBD plasma actuators can be installed.

The sound generation mechanism, known as thermophone, was discovered using a platinum membrane much earlier (1917)[9] but has not been widely utilized due to the relatively large power required for a

---

[*]Graduate Research Assistant, Department of Mechanical Engineering and Florida Center for Advanced Aero-Propulsion, cy13d@my.fsu.edu.

[†]Graduate Research Assistant, Department of Mechanical Engineering and Florida Center for Advanced Aero-Propulsion, pmm06d@my.fsu.edu.

[‡]Assistant Professor, Department of Mechanical Engineering and Florida Center for Advanced Aero-Propulsion, ktaira@fsu.edu.

[§]Aerospace Engineer, Vehicle Technology Directorate, matthew.j.munson6.civ@mail.mil

American Institute of Aeronautics and Astronautics

given sound pressure level. Compared to conventional metal membranes, the carbon-based (carbon nanotubes/graphene) membrane in consideration here can be fabricated extremely thin such that its heat capacity per unit area (HCPUA) is at least two orders of magnitude smaller than that of the metal . Since the output acoustic power delivered to the surrounding flow field is related inversely to the material HCPUA, C_{pua} (i.e., $P_{\text{output}} \propto C_{\text{pua}}^{-1} P_{\text{input}}$), the use of carbon-based material dramatically enhances the device efficiency. According to the measurements reported in Tian $et\ al.$[6] and Lin $et\ al.$,[10] the carbon-based devices are able to deliver constant noise levels of ≈ 85 dB, based on a reference sound pressure of 20 μPa and 5 cm distance for a 1 cm $\times$ 1 cm speaker, over a broad range of frequency, 10-50 kHz, which should be of interest for many flow control applications.[11]

Past studies have shown that inherent acoustic feedback mechanisms in flow over a cavity[12] or impinging jet[13] yield significantly different flow behavior compared to cases without the presence of such feedback path. There are also reports of acoustic perturbation being able to modify the flow over airfoils[14] or stabilize combustion instabilities[15] from external acoustic input (not attached to the body surface). We however re-emphasize that past acoustic actuators could not be readily mounted on the surface of bodies due to their size (including synthetic jets that relies mostly on momentum injection). The present study will examine how strong acoustic perturbation introduced locally can alter the flow field based on a surface-mounted thermoacoustic actuator.

The objective of the present study is to gain insights into how thermoacoustic actuators based on carbon nanotubes/graphene can alter turbulent separated flows. A boundary condition model[16] that captures the generation of thermoacoustic waves is implemented in the LES for flow over a wall-mounted hump to examine the influence of thermoacoustic perturbation on reducing drag and altering the profile of the recirculation bubble. The hump geometry is chosen from the NASA Validation Workshop,[17–20] shown in Figure 1. The use of this hump geometry facilitates the base flow validation and the comparison of the thermoacoustic flow control mechanism against other types of actuators. This specific problem is chosen to assess the performance of high-intensity acoustic waves for turbulent flow modification.

II. Simulation Approach

Large Eddy Simulation (LES) of the turbulent flow field over the wall-mounted hump is performed using the Vreman model with CharLES,[21–23] which is a compressible flow solver with second-order accuracy in space and third-order accuracy in time. Throughout this work, $Re \equiv \rho_\infty U_\infty c/\mu_\infty = 0.5 \times 10^6$ and $M_\infty \equiv U_\infty/a_\infty = 0.25$ are chosen to match representative cases considered in the NASA Validation Workshop.[18–20] The computational domain size is also chosen to match the experimental setup given by the workshop guidelines[17] and the study conducted by Greenblatt $et\ al.$[24] The streamwise extent is $x/c \in [-2.14, 4]$ with the hump positioned from $x/c = 0$ to 1, as illustrated in Figure 1. The vertical extent of the domain is $y/c \in [0, 0.909]$ with the region above the hump lowered to introduce a contraction which helps capture the blockage effect of the side splitter plates in the experiments.[17] The spanwise direction is taken to be periodic with an extent of $z/c \in [0, 0.2]$. The spatial domain is discretized with a structured grid with a near-wall grid resolution of $\Delta x^+ = u_\tau \Delta x/\nu = 25$, $\Delta y^+ = 0.25$, $\Delta z^+ = 15$ around the hump. The overall grid size is 93×10^6 for the both baseline and the controlled cases.

The inlet boundary condition is specified to match the experimental measurement of the boundary layer profile reported in the workshop guidelines[17] and Greenblatt $et\ al.$[24] By adding fluctuation of random Fourier modes[25,26] to the inlet profile, the turbulent intensity is also ensured to be matched at the inlet such that the turbulence is allowed to develop before reaching the leading edge of the hump. No-slip boundary condition is applied along the wall boundary (bottom), whereas no-stress boundary condition is imposed on the top boundary. A first-order up-winding scheme is applied away from the hump $y > 0.25$ to damp out the exiting waves. Along the outlet, we utilize the sponge zone to damp out any outgoing acoustic waves or exiting vortical structures.[27]

Validation

The present calculation is validated by comparing the baseline separated flow over the hump with the experimental measurements of Seifert and Pack[18] ($M_\infty = 0.25$, $Re_\infty = 2.4$ to 26×10^6), Greenblatt $et\ al.$[24] ($M_\infty = 0.1$, $Re_\infty = 1 \times 10^6$) and the numerical results of Franck and Colonius[20] ($M_\infty = 0.25$, $Re_\infty = 0.6 \times 10^6$). Shown in Figure 2 is the baseline pressure coefficient $c_p \equiv (p - p_\infty)/(\frac{1}{2}\rho_\infty U_\infty^2)$, which agrees well

American Institute of Aeronautics and Astronautics
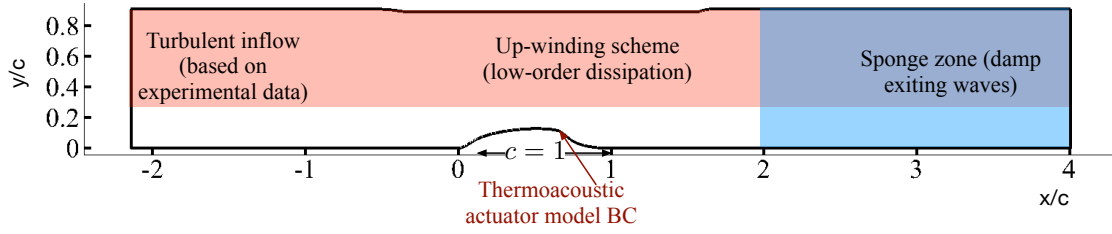
Figure 1: Geometry of the computational domain (xy-plane). The spanwise (z) extent is 0.2 for three-dimensional computations. Turbulent inflow condition is specified at the inlet. Up-winding and the sponge zone are utilized to allow waves to leave the domain without numerical reflections.

with other experimental measurements over the hump. Reasonable agreement between our result and the numerical calculation by Franck and Colonius[20] is also observed. The slight difference may be attributed to the larger grid size in the present calculation than that was used by Franck and Colonius. The time-average velocity profiles and Reynolds stress distribution are presented in Figure 3, showing good agreement with the PIV measurements of Greenblatt et $al.$[24] and computational findings of Franck and Colonius.[20] From these results, it has been observed that there are many common traits in the separated flow at these Reynolds numbers ($Re_\infty = 0.5 \times 10^6$ and 1×10^6) and Mach numbers ($M_\infty = 0.1$ and 0.25). For the chosen grid resolution and domain setup, the baseline results are found to be in agreement with those reported in past studies. The validated baseline simulation provides us with the test bed to explore the use of thermoacoustic flow control on the wall-mounted hump problem.
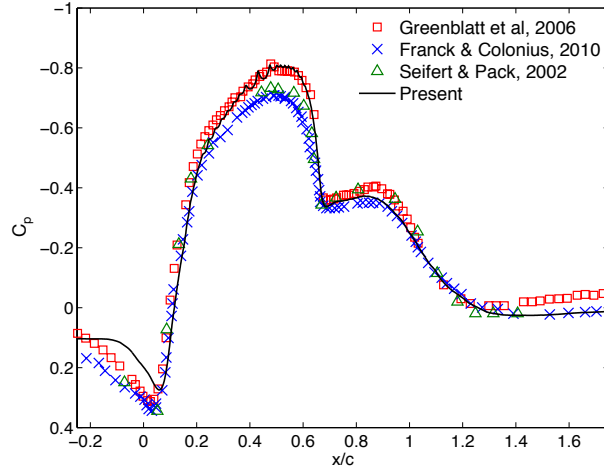
Figure 2: Comparison of baseline pressure distribution over the hump.

III. Thermoacoustic Actuator

The generation of acoustic waves from graphene/carbon-nanotube based actuators is modeled by a thermal boundary condition in the present LES. A sinusoidal heat flux $q_{\text{wall}} = \hat{q}\big[1+\sin(2\pi ft)\big]\cos\big((x-x_a)\pi/\sigma\big)$, (where $|x - x_a| \leq \sigma/2$ and $\hat{q} \ll 1$) is used to represent the thermoacoustic actuator, which is positioned at $x_a/c = 0.6563$ near the separation point as a spanwise strip with a width σ of $\sigma/c = 4.4 \times 10^{-3}$. The position and width are selected to be the same as the width of the synthetic jet actuator slot used in the NASA validation study. The actuation frequency f is non-dimensionalized and represented by the Helmholtz number defined as $\text{Hn} = 2\pi f\sigma/a_\infty$, where a_∞ is the free stream acoustic speed. Helmholtz number is used

American Institute of Aeronautics and Astronautics
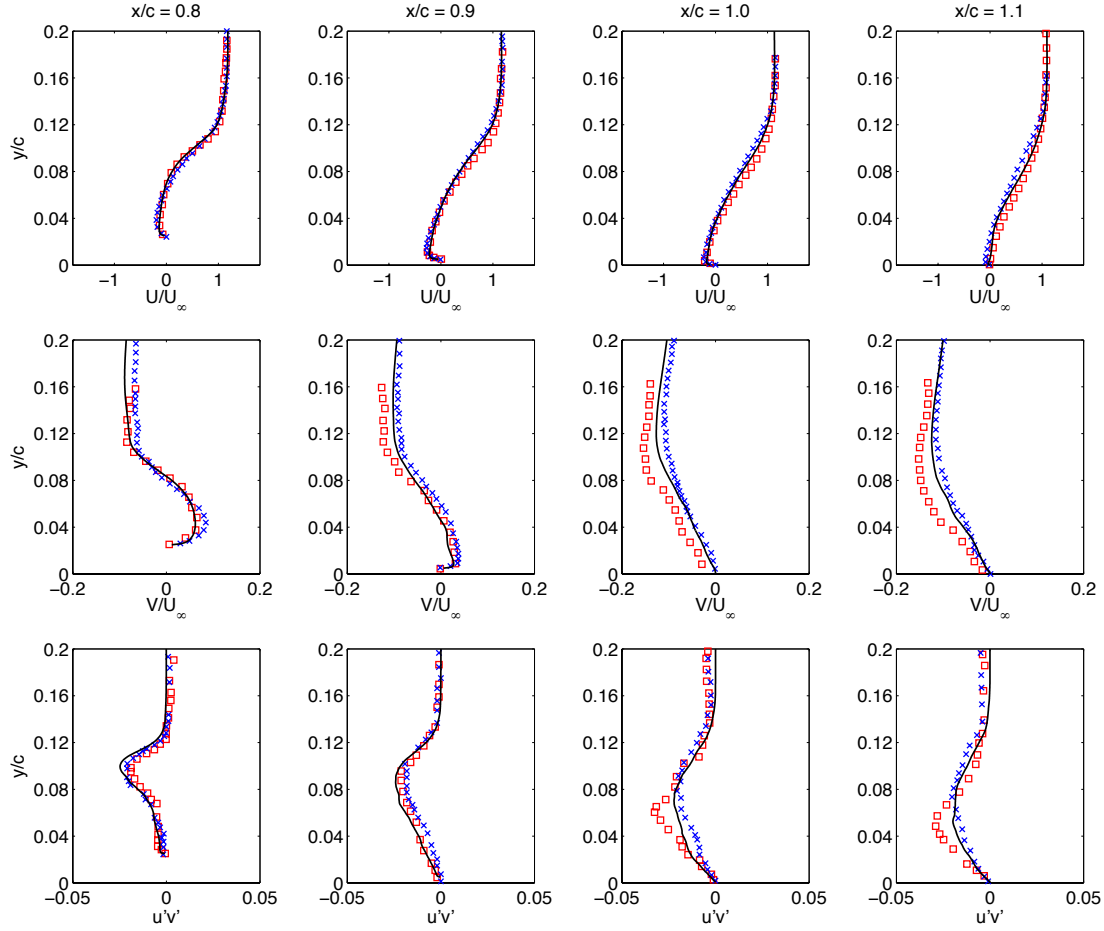
Figure 3: Comparison of time-average velocity and Reynolds stress for the baseline three-dimensional flow. □ : Greenblatt *et al.*, 2006; × : Franck & Colonius, 2010; ———— : present.

as a non-dimensionalized frequency throughout this work since we aim to examine the effectiveness of the actuation frequency based on the order of sonic speed rather than that based on hydrodynamic shedding frequency, which is usually characterized by the Strouhal number.

The validity of the heat flux boundary condition is examined on the hump in a two-dimensional domain with a quiescent condition using an actuation frequency that corresponds to the Helmholtz number $Hn = 3$ based on the actuator characteristics reported by Tian *et al.*,[6] and an amplitude of $\hat{q} = 1.53 \times 10^{-3}$. The pressure field generated from this actuator is shown in Figure 4 (left). The sound pressure is also monitored at the location 5σ away normal from the hump surface at various values of $\hat{q}$ and actuation Hn. The spectra of representative cases are also shown in Figure 4 (right), where peak amplitude is presented at each prescribed actuation Helmholtz number. With lower Hn and lower $\hat{q}$, their magnitudes are observed to decrease. The measured SPL is plotted against $\hat{q}$ in Figure 5 (left) and against prescribed actuation Hn (right). The revealed relationships between SPL and the input power $\hat{q}$, as well as that between SPL and actuation frequency, agree with those reported by Tian *et al.*,[6] who acquired measurements from a square area of actuator rather than a stripe arrangement. We also note that the drag and lift (coefficients) directly generated by actuation in quiescent flow are of $\mathcal{O}(10^{-6})$, which are practically negligible compared to the aerodynamic force exerted by the flow over the hump to be controlled.

The result shows that the present thermal boundary condition that models the thermoacoustic actuator predicts the characteristics of the emitted acoustic waves reasonably well. Hence, we use the above heat flux boundary condition in the active flow control simulations shown below.

American Institute of Aeronautics and Astronautics
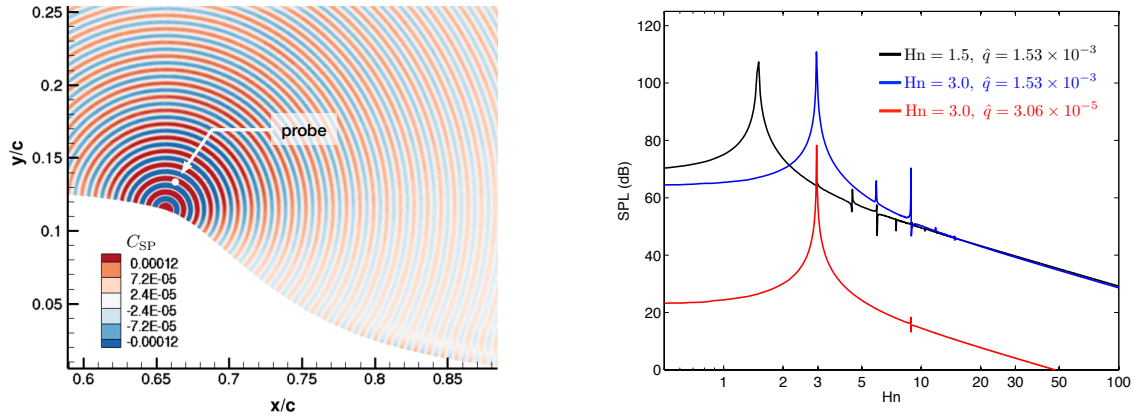
Figure 4: LES pressure contour of two-dimensional thermoacoustic waves generated from a sinusoidal heat flux input on the hump, where $C_{\text{sp}} \equiv (p - p_\infty)/(\frac{1}{2}\rho_\infty a_\infty^2)$, on the left. SPL is 112 dB at the probe location. Sound pressure spectrum of selected actuation Hn is on the right.
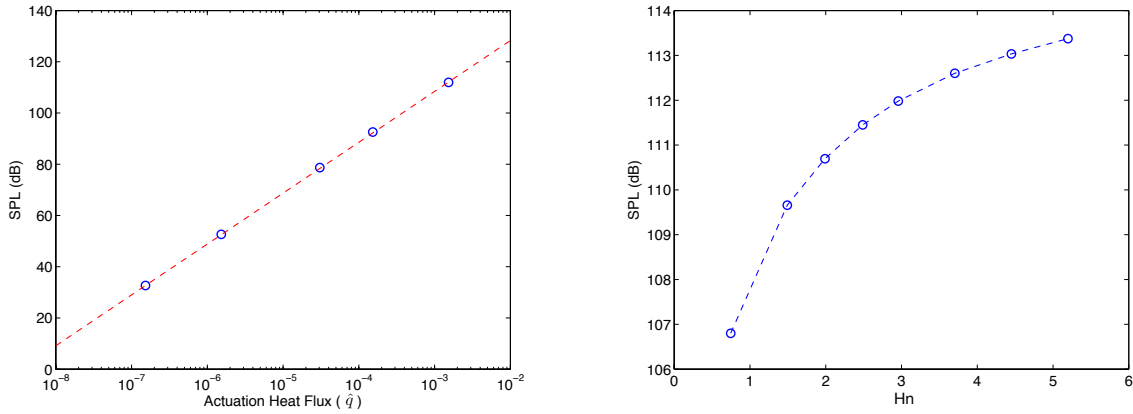
Figure 5: LES sound pressure at 5σ away (probe location) from the actuator. SPL at this point is plotted against the heat flux input, $\hat{q}$, on the left, and against actuation Helmholtz number, Hn, on the right.

IV. Results

We present results from two and three-dimensional LES with thermoacoustic boundary condition applied for active flow control. Below we compare and contrast the difference between the uncontrolled and controlled turbulent flow fields and discuss how the exerted aerodynamic force is altered. First, two-dimensional simulations are performed to examine whether acoustic flow control can alter the flow field. Next, three-dimensional LES with Hn = 3 and SPL of 110 dB is considered. The acoustically controlled flow shows favorable results in reducing the drag on the wall-mounted hump for both two and three-dimensional cases.

Hn	SPL (dB)	C_D (10^{-2})	C_{FD} (10^{-2})	C_{VD} (10^{-2})	ΔC_D
2D Cases					
Baseline	$--$	5.259	5.131	0.1286	$--$
0.3	110	5.241	$+0.034$	-0.0005	$+0.63\%$
0.5	110	5.313	$+0.080$	$+0.0005$	$+1.53\%$
1.0	110	4.878	-0.071	$+0.0016$	-1.32%
1.5	110	5.563	$+0.302$	$+0.0023$	$+5.79\%$
2.0	110	4.215	-0.098	$+0.0048$	-1.77%
3.0	110	5.033	-0.230	$+0.0035$	-4.31%
4.5	110	5.324	-0.070	$+0.0035$	-1.26%
3.0	80	5.554	$+0.298$	-0.0027	$+5.60\%$
3.0	50	5.257	-0.023	$+0.0008$	-0.41%
3D Cases					
Baseline	$--$	3.272	2.983	0.289	$--$
3	110	3.065	-0.205	-0.002	-6.33%

Table 1: Control setups and the coresponding drag change in total drag, C_D, form drag, C_{FD} and viscous drag, C_{VD}. The drag change ΔC_D is defined as $\left(C_{D,\text{ controlled}} - C_{D,\text{ baseline}} \right) / C_{D,\text{ baseline}}$.
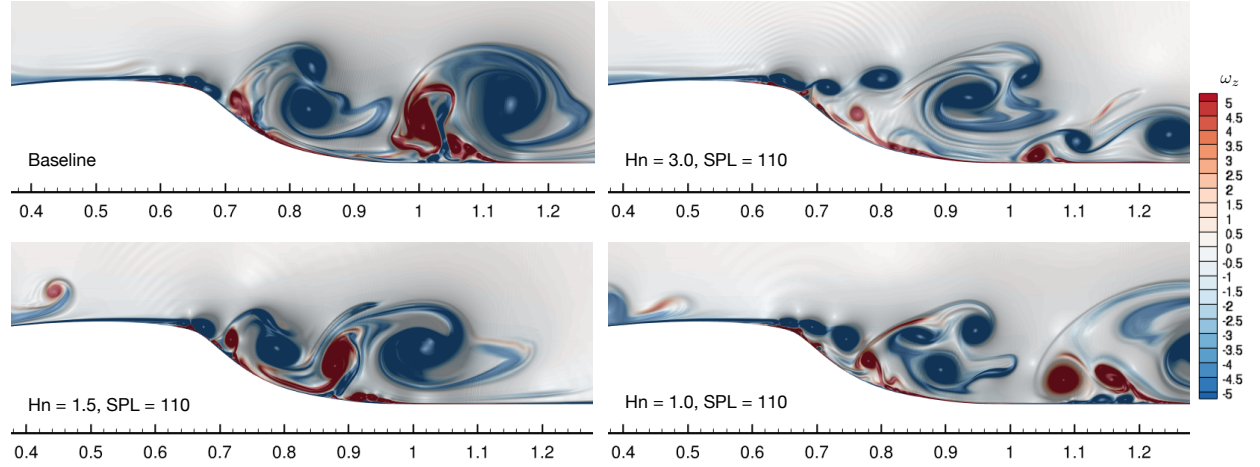
Two-Dimensional Flow

We consider two-dimensional flow field interacting with high-intensity acoustic waves. The computational domain is the same as three-dimensional simulations but with only a single control volume in the spanwise direction. This renders the grid size to be 0.58×10^6 for the two-dimensional calculation. Including the baseline, simulations with ten actuation parametric sets are performed, as listed in Table 1. The actuation Hn ranges from 0.3 to 4.5, and two lower values of $\hat{q}$ are also chosen to generate SPL of 80 and 50 at actuation Hn = 3. For each case, simulation is carried out for at least 60 chord convective units. Also reported in Table 1 are the time-average total drag coefficient, C_D, form drag coefficient, C_{FD}, viscous drag coefficient C_{VD} and the percentage change in total drag coefficient comparing to the baseline value. All these numbers are time-averaged over 50 convective units after the transient of first streamwise domain length has been washed out by the free stream. Following, we present the flow fields of the baseline flow along with three selected actuated cases, which are shaded in Table 1. Note that the case with actuation Hn = 1.5 gives drag increase and, as will be pointed out shortly, the flow field feature is distinctive to the other two cases where drag is reduced.

The instantaneous spanwise vorticity contours as well as the numerical Schlieren are shown in Figure 6 for both the uncontrolled and controlled cases. Due to the absence of spanwise variation, two-dimensional simulation reveals larger spanwise vortices forming and shedding from the wall-mounted hump. With high-frequency acoustic perturbations added, the spanwise vortices appear to become smaller in cases of actuation Hn of 1.0 and 2.0 compared to the baseline, but have no obvious decrease in size with actuation Hn of 1.5. In the numerical Schlieren images, the emitted acoustic waves can be seen for every case with SPL $\approx$ 110, and

American Institute of Aeronautics and Astronautics

greater wave length is observed for lower actuation Hn. We also observe the generation of smaller opposite sign vortices near the wall. The acoustic perturbations appear to create small-scale structures that trigger the roll-up of smaller vortices behind the hump. The smaller vortical structure leads to the decrease in the spanwise Reynolds stress as shown in Figure 7, which suggests the turbulent intensity is also decreased when effective actuation frequency is introduced.

The corresponding time-averaged pressure contour and streamlines are plotted in Figure 8, which shows the recirculation region is elongated in those cases with drag reduction. This can be explained as a consequence of the change in time-averaged spanwise vorticity shown in Figure 9 (right). With the contour of $\omega_z = -3$ plotted, we observe that the spanwise vorticity is transported (convected) further downstream with actuation frequency of Hn = 1.0 and 3.0. This allows the sheet to convect downstream and delays the growth of large-scale instability, and leads to the elongation of circulation zone in the streamwise direction. Also shown in Figure 9 (left) are the contours of $\bar{C}_p = -1.024$. This shows the low pressure core reduced and shifted away from the hump leading to the decrease in drag.
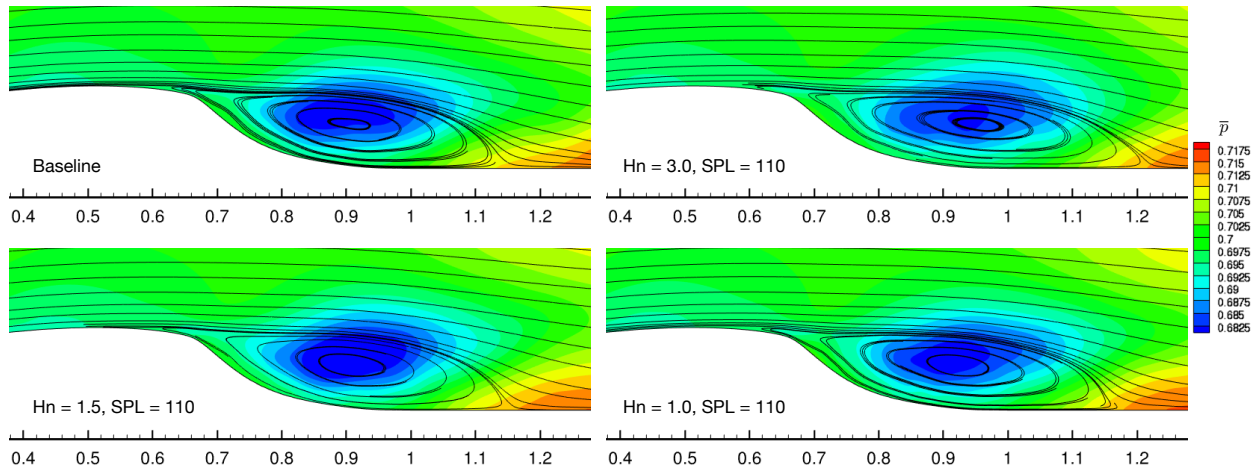

Figure 6: Instantaneous vorticity and numerical Schlieren of the two-dimensional controlled flow for different actuation conditions.
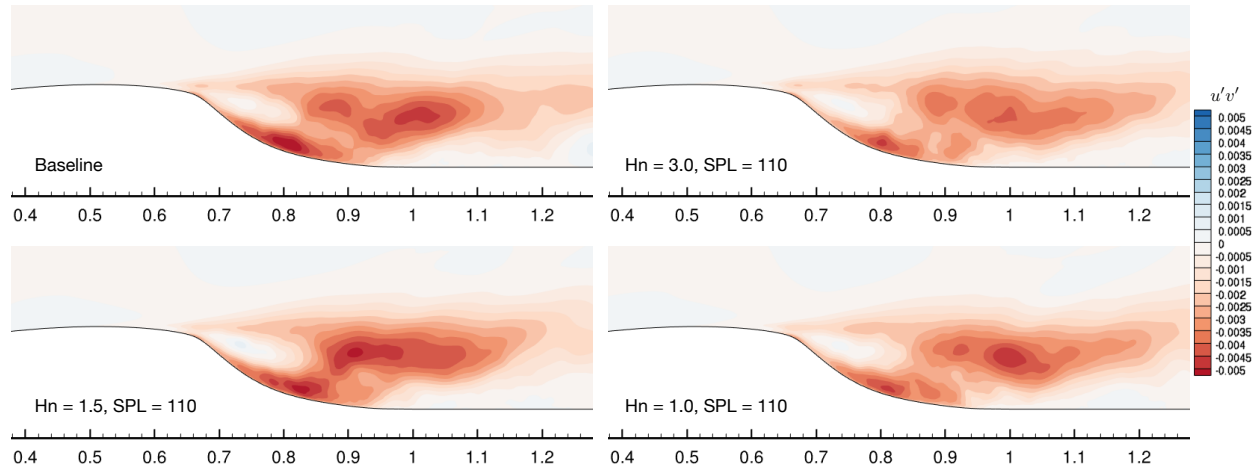

Figure 7: Spanwise Reynolds stress $(u'v')$ for the two-dimensional controlled flow in different actuation conditions.

The elongation of the recirculation region correlates with the cases with the largest reduction in drag, as seen in Table 1. Since the low-pressure core is pushed further downstream, the drag force on the hump is decreased. The pressure coefficient over the hump is plotted in Figure 10. We note that upstream of the separation point there appears to exhibit only minor differences between the baseline and the actuation

American Institute of Aeronautics and Astronautics

Figure 8: Time-average streamlines and pressure for the two-dimensional controlled flow for different actuation conditions.
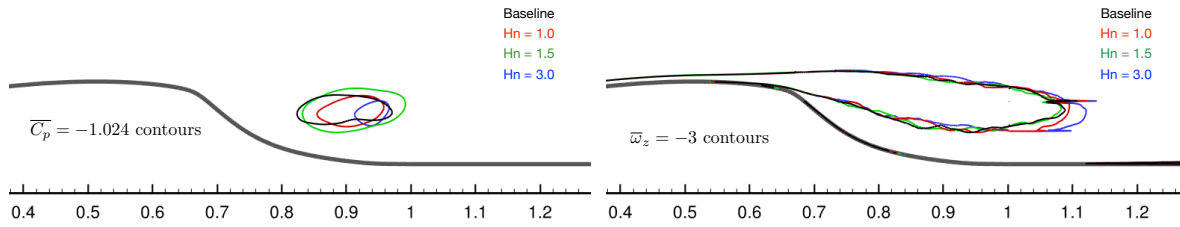
Figure 9: Time-average vorticity and pressure contours of the two-dimensional controlled flow at different actuation conditions.

cases. This suggests us that the drag reduction comes from the modifications made to the wake. The acoustic flow control is able to reduce the drag on the hump by up to 4.31% for two-dimensional flow. The wake elongation used for drag reduction is of the opposite trend from how synthetic jet controls the flow over the hump in past studies. With synthetic jets, recirculation zones are reduced in size for recovering pressure loss to achieve drag reduction.

Spectrum of drag is also shown in Figure 11, where the decease of dominant peak amplitudes for the controlled case is observed. The actuation frequencies, Hn = 1.0, 1.5 and 3.0 can be seen to be of very limited spectral power. The use of acoustic perturbation does not directly shift the flow, but appears to trigger instability differently to the controlled flow that alters the global flow field. This approach shares similarity with the flow control on a jet using high-frequency piezoelectric actuator performed by Wiltse and Glezer.[11]
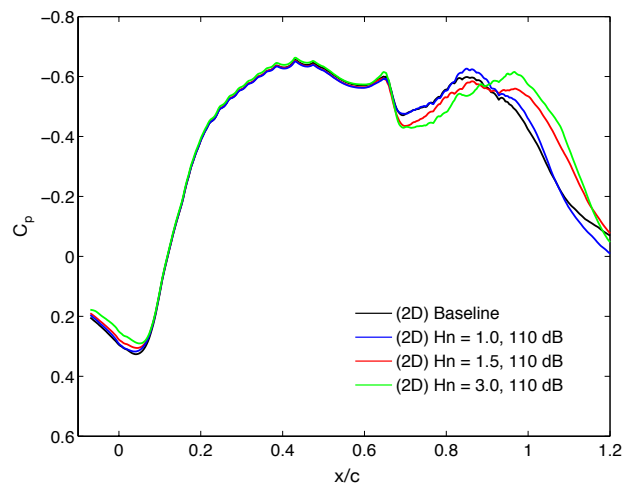
Three-Dimensional Flow

Next, we consider the effect of high-intensity acoustic waves on three-dimensional turbulent flow over the hump. Due to the large computational time required to perform the LES calculation on the DoD HPC cluster, we have limited our controlled simulation to a single case with Hn = 3 and SPL of 110 dB.
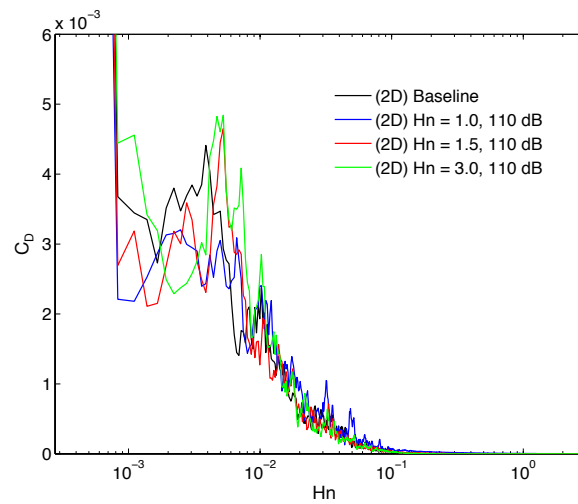
The instantaneous three-dimensional flow fields from the baseline and controlled cases are shown in Figure 12. The controlled simulation required fine grid resolution around the actuator location to resolve the interaction between the acoustic waves and the turbulent structures. This renders overall grid size for the controlled flow to be 93 million points. We believe both the uncontrolled and controlled cases are resolved well since the baseline case has been well validated as discussed earlier and the vortical wake structures in both cases are well-captured. For the controlled flow, the acoustic waves are also well resolved as it can be seen in the numerical Schlieren in the background of Figure 13.

In Figure 12, we notice that the turbulent flow structures become finer with acoustic control input. As a consequence of smaller turbulent structures, the amplitude of fluctuation is reduced and the turbulent

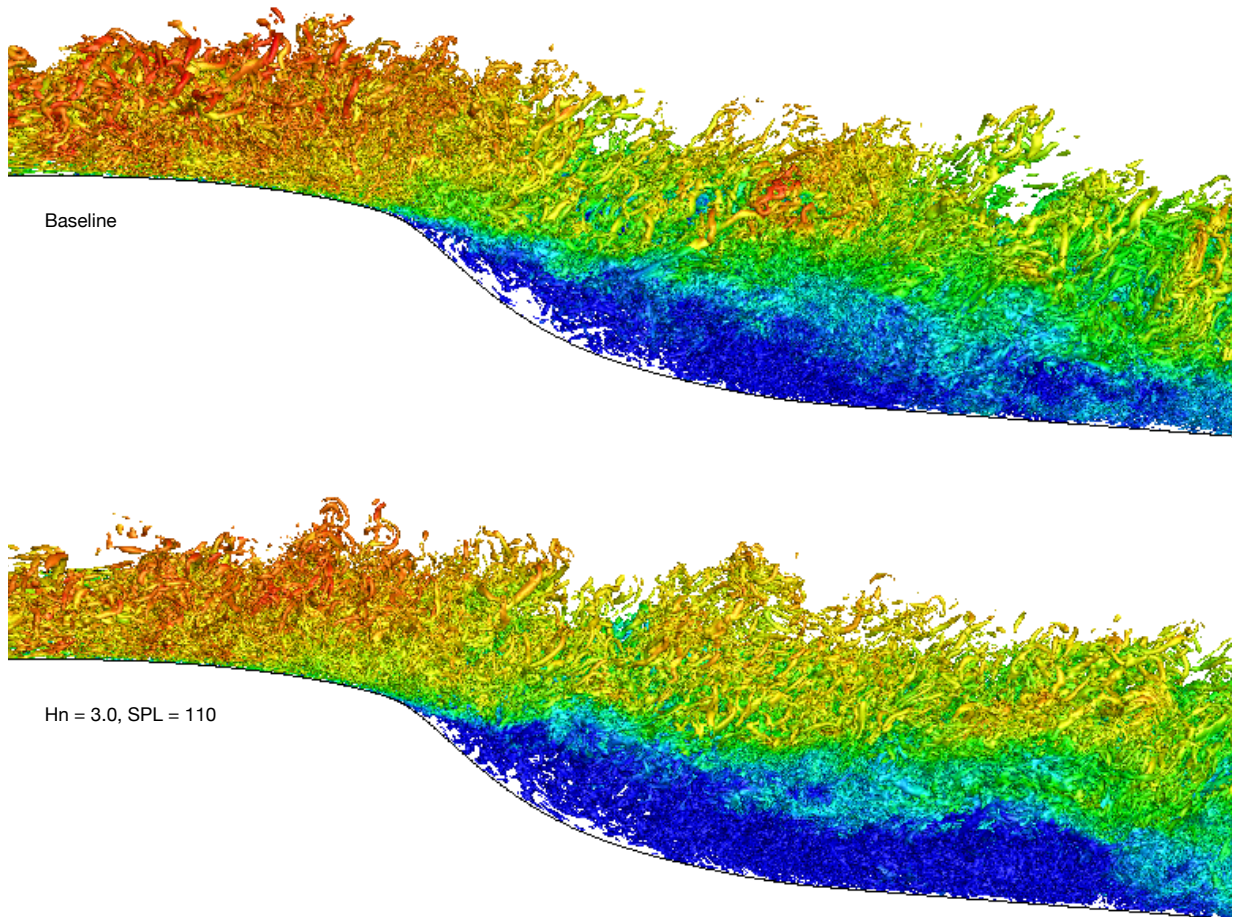American Institute of Aeronautics and Astronautics

**Figure 10:** Time-averaged pressure coefficient over the hump for two-dimensional controlled flow.

Figure 11: Drag spectra with flow control of two-dimensional flow.

Figure 12: Comparison of the baseline and acoustically controlled (Hn = 3.0) instantaneous flow fields downstream of the wall-mounted hump. Three-dimensional structures are visualized by the Q-criterion colored with streamwise velocity. The turbulent structures are smaller with elongated wake for the controlled flow using high-intensity acoustic waves.
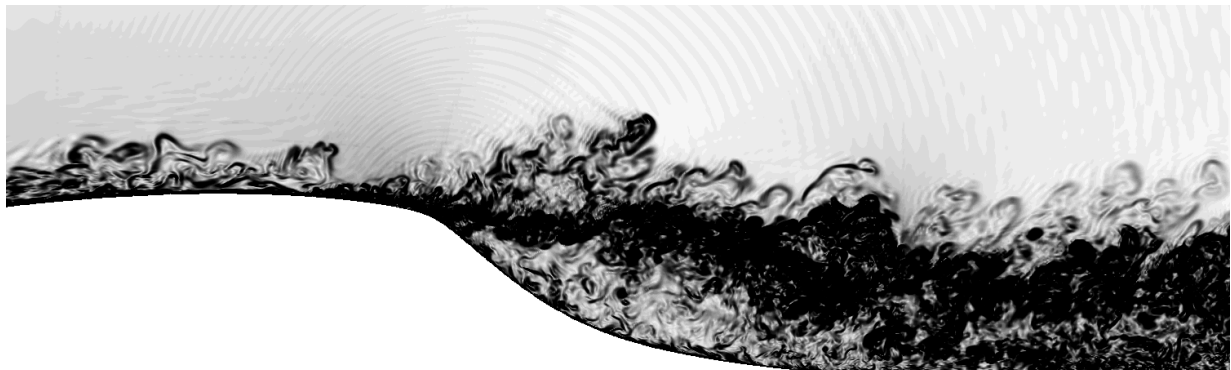

Figure 13: Numerical Schlieren of the three-dimensional controlled flow with an actuation frequency of Hn = 3.0.

American Institute of Aeronautics and Astronautics
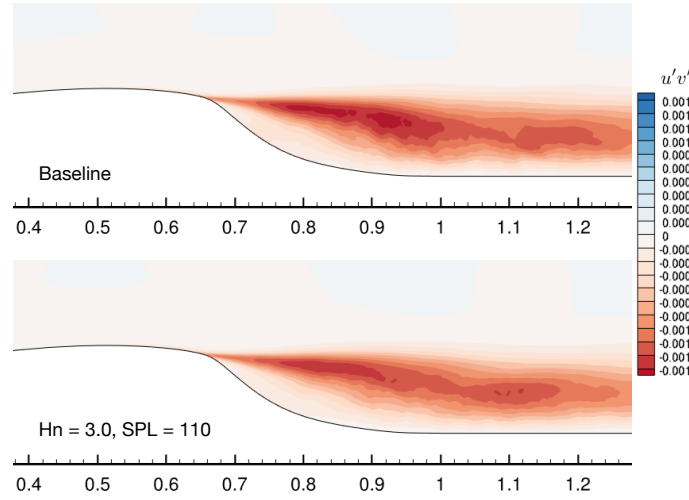
Figure 14: Spanwise Reynolds stress for three-dimensional simulation. The turbulent intensity is mitigated in the controlled case.

intensity is also decreased, which can be seen in Figure 14. We can also observe from Figure 12 that the wake is elongated with acoustic control. The large blue region (low velocity region) is prominent in the controlled case as the separated region extends further downstream of the hump. This wake elongation for three-dimensional flow can be seen more clearly from Figure 15. The recirculation zone for the controlled case is found to elongate by approximately 9% compared to the baseline case. As depicted in Figure 16 (left), this elongation also shifts the low-pressure region associated with the wake downstream and leads to drag reduction as noted in Table 1. In the absence of large scale vortical structure, the shear layer is stabilized and allows the spanwise vorticity convected further downstream, which is also shown in the comparison of time-average vorticity contours for baseline and control case in Figure 16. All these observations are aligned with those made for two-dimensional flow discussed above.
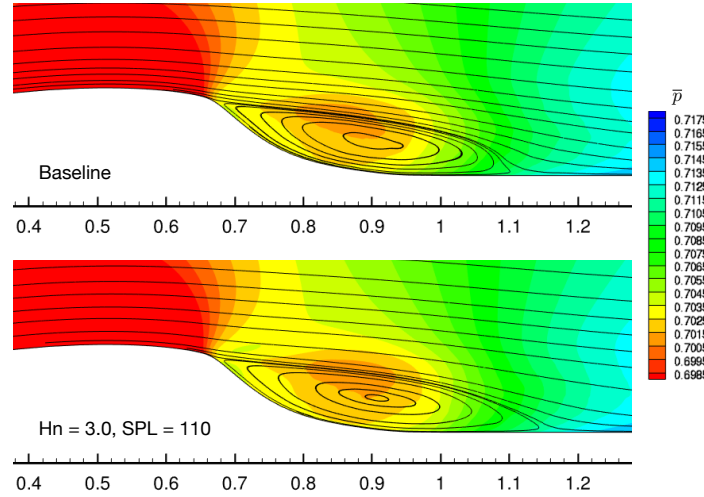

Figure 15: Time-averaged streamlines for baseline (top) and the actuated case (bottom) for three-dimensional flow.

V. Drag Reduction and Control Efficiency

With the observation from the two and three-dimensional flow fields, we conclude that the change in drag coefficient can be mostly attributed to the pressure effect, that is, the change in form drag. This is also shown in Table 1 as well as in Figure 17. For two-dimensional computations, where we have nine different actuation Hn, the change in viscous drag is negligible compared to the change of in form drag, leaving the total drag
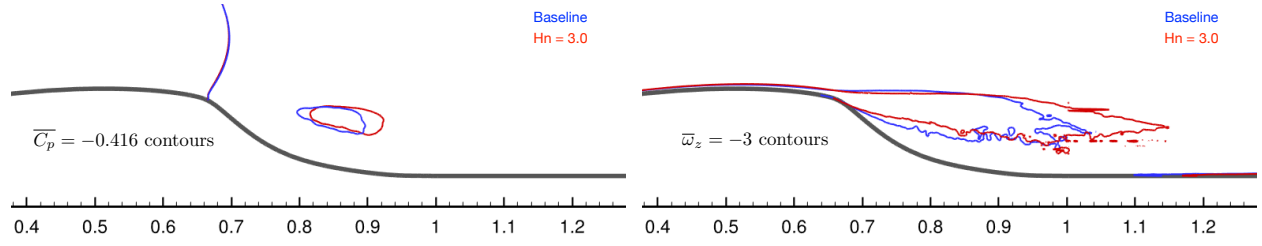
Figure 16: Time-average pressure (left) and vorticity (right) contours of the three-dimensional baseline and controlled flow.
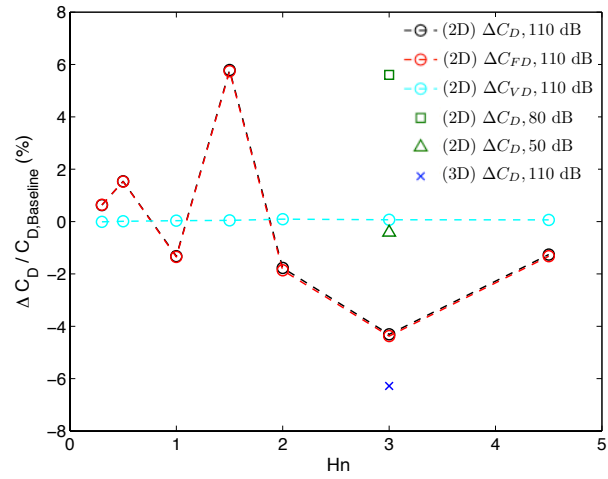
Figure 17: Change in drag coefficient of all actuation setups.

change data points, ΔC_D, collapsing with those of form drag change, ΔC_{FD}, as show in Figure 17. The change in drag appears to depend on control inputs, including actuation frequency and amplitude. For the actuation setups that have been explored in current work, the Helmholtz number of 3.0 achieves the largest drag reduction. Furthermore, a larger drag decease of 6.33% from the three-dimensional LES is achieved than from the two-dimensional calculation. This can be attributed to a currently hypothesized mechanism of the acoustic drag reduction control: The acoustic wave appears to trigger instabilities that break apart large vortical structures into smaller ones and, in the mean while, suppress the formation of large structures to form. Correspondingly, without large scale vortical shedding in the wake, the shear layer becomes more stable, leading to an elongated recirculation zone, and hence reduce the drag. For the three-dimensional flow, this proposed mechanism appears to be more effective than that seen in the two-dimensional simulation, and thus higher reduction in drag is observed.

To make sure the investment in the power input on the thermoacoustic actuator drag is profitable, we compare it to the decrease in drag power. According to the oscillatory heat flux boundary condition that models the thermoacoustic actuator (described in Section III), the power input, $\dot{Q}$, can be calculated by integrating q_{wall} over the actuator stripe and taking the average over one oscillation period. This gives $\dot{Q} = 2\sigma\hat{q}/\pi$. Now we can define the drag reduction control efficiency E as $E = \frac{1}{2}\rho_\infty U_\infty^3 \Delta C_D / \dot{Q}$. Using the magnitude of drag decrease from three-dimensional simulation, we have $E = 3.74 > 1$. This suggests the applicability of drag reduction control using the developed low power-consumption thermoacoustic actuators appears promising.

Acknowledgments

References

[1] Joslin, R. D. and Miller, D. N., editors, *Fundamentals and applications of modern flow control*, AIAA, 2009.

[2] Cattafesta, L. N. and Sheplak, M., "Actuators for active flow control," *Annu. Rev. Fluid Mech.*, Vol. 43, 2011, pp. 247–272.

[3] Glezer, A. and Amitay, M., "Synthetic jets," *Annu. Rev. Fluid Mech.*, Vol. 34, 2002, pp. 503–529.

[4] Corke, T. C., Enloe, C. L., and Wilkinson, S. P., "Dielectric barrier discharge plasma actuators for flow control," *Annu. Rev. Fluid Mech.*, Vol. 42, 2010, pp. 505–529.

[5] Crittenden, T. M. and Raghu, S., "Combustion powered actuator with integrated high frequency oscillator," *Int. J. Flow Control*, Vol. 1, 2009, pp. 87–97.

[6] Tian, H., Ren, T.-L., Xie, D., Wang, Y.-F., Zhou, C.-J., Feng, T.-T., Fu, D., Yang, Y., Peng, P.-G., Wang, L.-G., and Liu, L.-T., "Graphene-on-Paper Sound Source Devices," *ACS Nano*, Vol. 5, No. 6, 2011, pp. 4878–4885.

[7] Hu, H., Zhu, T., and Xu, J., "Model for thermoacoustic emission from solids," *App. Phys. Let.*, Vol. 96, 2010, pp. 214101.

[8] Baloch, K. H., Voskanian, N., Bronsgeest, M., and Cumings, J., "Remote Joule heating by a carbon nanotube," *Nature Nanotechnology*, Vol. 7, May 2012, pp. 316–319.

[9] Arnold, H. D. and Crandall, I. B., "The Thermophone as a Precision Source of Sound," *Phys. Rev. B*, Vol. 10, 1917, pp. 22–38.

[10] Xiao, L., Chen, Z., Feng, C., Liu, L., Bai, Z.-Q., Wang, Y., Qian, L., Zhang, Y., Li, Q., Jiang, K., and Fan, S., "Flexible, stretchable, transparent carbon nanotube thin film loudspeakers," *Nano Letters*, Vol. 8, No. 12, 2008, pp. 4539–4545.

[11] Wiltse, J. M. and Glezer, A., "Direct excitation of small-scale motions in free shear flows," *Phys. Fluids*, Vol. 10, No. 8, 1998, pp. 2026–2036.

[12] Rockwell, D. and Knisely, C., "The organized nature of flow impingement upon a corner," *J. Fluid Mech.*, Vol. 93, No. 3, 1979, pp. 413–432.

[13] Tam, C. K. W. and Ahuja, K. K., "Theoretical model of discrete tone geenration by impinging jets," *J. Fluid Mech.*, Vol. 214, 1990, pp. 67–87.

[14] Zaman, K. B. M. Q., Bar-Sever, A., and Mangalam, S. M., "Effect of acoustic excitation on the flow over a low-Re airfoil," *J. Fluid Mech.*, Vol. 182, 1987, pp. 127–148.

[15] Lang, W., Poinsot, T., and Candel, S., "Active control of combustion instability," *Comb. Flames*, Vol. 70, No. 3, 1987, pp. 281–289.

[16] Bin, J., Oates, W. S., and Taira, K., "Thermoacoustic modeling and uncertainty analysis of two-Dimensional conductive membranes," *J. App. Phys.*, 2014 in review.

[17] Sellers, W. L. and Rumsey, C. L., "Langley Research Center Workshop: CFD Validation of Synthetic Jets and Turbulent Separation Control, 2004," .

[18] Seifert, A. and Pack, L. G., "Active Flow Separation Control on Wall-Mounted Hump at High Reynolds Numbers," *AIAA J.*, Vol. 40, No. 7, 2002, pp. 1363–1372.

[19] Rumsey, C. L., "Proceedings of the 2004 Workshop on CFD Validation of Synthetic Jets and Turbulent Separation Control," Tech. Rep. NASA/CP-2007-214874, NASA, 2007.

[20] Franck, J. A. and Colonius, T., "Compressible Large-Eddy Simulation of Separation Control on a Wall-Mounted Hump," *AIAA J.*, Vol. 48, No. 6, 2010, pp. 1098–1107.

[21] Khalighi, Y., Nichols, J. W., Ham, F., Lele, S. K., and Moin, P., "Unstructured Large Eddy Simulation for Prediction of Noise Issued from Turbulent Jets in Various Configurations," 17th AIAA/CEAS Aeroacoustics Conference, 2011.

[22] Khalighi, Y., Ham, F., Moin, P., Lele, S., Schlinker, R., Reba, R., and J., S., "Noise Prediction of Pressure-Mismatched Jets Using Unstructured Large Eddy Simulation," Proceedings of ASME Turbo Expo, Vancouver, 2011.

[23] Brés, G. A., Nichols, J. W., Lele, S., and Ham, F. E., "Towards Best Practices for Jet Noise Predictions with Unstructured Large Eddy Simulations," 42nd AIAA Fluid Dynamics Conference, New Orleans, 2012.

[24] Greenblatt, D., Paschal, K. B., Yao, C.-S., Harris, J., Schaeffer, N. W., and Washburn, A. E., "Experimental investigation of separation control. Part 1: baseline and steady suction," *AIAA J.*, Vol. 44, No. 12, 2006, pp. 2820–2830.

[25] Béchara, W., Bailly, C., Lafon, P., and Candel, S. M., "Stochastic approach to noise modeling for free turbulent flows," *AIAA J.*, Vol. 32, No. 3, 1994, pp. 455–463.

[26] Franck, J. A., *Large-Eddy simulation of flow separation and control on a wall-mounted hump*, Ph.D. thesis, California Institute of Technology, 2009.

[27] Freund, J. B., "Proposed inflow/outflow boundary condition for direct computation of aerodynamic sound," *AIAA J.*, Vol. 35, No. 4, 1997, pp. 740–742.